Surface grain orientation mapping using grazing incidence X-ray diffraction

(article starts on next page)

Contents lists available at ScienceDirect

Surface Science

Surface grain orientation mapping using grazing incidence X-ray diffraction

Hanna Sjö [a],[*] , Anatoly Shabalin [b], Ulrich Lienert [b], Johan Hektor [c], Andreas Schaefer [d],
Per-Anders Carlsson [d], Carl Alwmark [e], Johan Gustafson [a]

[a] Department Physics, Lund University, Box 118, Lund 221 00, Sweden
[b] DESY Photon Science, Hamburg 22607, Germany
[c] Department of Materials Science and Applied Mathematics, Malmö University, SE-205 06, Malmö, Sweden
[d] Department of Chemistry and Chemical Engineering, Chalmers University of Technology, Kemigården 4, Gothenburg 412 96, Sweden
[e] Department of Geology, Lund University, Sölvegatan 12, Lund 22362, Sweden

ARTICLE INFO

ABSTRACT

Tomographic surface X-ray diffraction (TSXRD) is an adaptation of classic surface X-ray diffraction to allow for measurements of polycrystalline surfaces. Compared to most other surface-sensitive techniques, surface X-ray diffraction has advantages in *operando* studies, since it can provide crystallographic information about surface structures in high gas pressures (above atmospheric) as well as through liquids. The method has, however, so far been limited to ideal samples, such as single crystals, since the long beam footprint illuminates several grains, which, with conventional SXRD, prevents an assignment of the diffraction signal and thus the structural information, to a certain grain. Here, we present the first step in the development of TSXRD, in which the grain shapes and orientations on a polycrystalline surface can be mapped using grazing incidence X-ray diffraction. The resulting knowledge about the shape, position, and orientation of the grains at the surface will be the steppingstone for further SXRD analysis of polycrystalline surfaces, allowing us to identify which diffraction signals belong to which grain. This method is thus part of opening up SXRD as a method for *operando* studies of more industry-relevant samples. Our grain maps are compared to those obtained with electron back-scatter diffraction measurements of the same sample, confirming the validity of the method.

1. Introduction

A vital part of the transition towards a sustainable society is the development of functional materials, for example, catalysts, solar cells, and batteries [1–3]. For these applications, interactions with surfaces and across interfaces, such as the interaction between a catalytic surface and gas-phase reactants, play a crucial role and are, in turn, governed by the structure of these surfaces and interfaces [4–6]. The materials in question are often complex and multifaceted, operating in harsh environments [7,8], making them difficult to study in detail, especially at the surface. Traditionally, surface studies are most often performed on single crystal surfaces using electron-based methods, which require high or Ultra-High Vacuum (UHV). This results in large differences between the studied model systems and the corresponding industrial systems, referred to as the material and pressure gaps. In order to make surface science more relevant for industrial applications, it is important to develop methods that are able to bridge both of these gaps, and there have been a lot of advancements in the last decades. X-ray photoelectron

spectroscopy, for example, was previously limited to UHV, but an ambient pressure version has made it possible to measure at pressures of several 100 mbar [9]. Two imaging techniques that have previously been limited to UHV are Photoemission Electron Microscopy (PEEM) and Low-Energy Electron Microscopy (LEEM) but now both have been developed to operate under 10^{-5} mbar and 10^{-1} mbar, respectively [10, 11]. Methods that can now be applied under, at least, atmospheric pleasure are high-pressure scanning tunneling microscopy [12] and Surface X-ray Diffraction (SXRD) [13,14]. Among these, SXRD is unique in its ability to determine surface structures with a resolution down to the sub-Ångström level in gas as well as liquid environments.

SXRD has been used in many studies of industrially relevant catalytic surfaces [13–16]. However, its application is limited to simplified model samples such as single crystals due to the long beam footprint caused by the grazing angle of incidence required to achieve surface sensitivity. Industrial devices, however, are rarely single crystals but polycrystalline and thus expose many different surface orientations, all with different properties. Studying each surface separately as single crystals is highly

---

* Corresponding author.
  E-mail address: hanna.sjo@sljus.lu.se (H. Sjö).

inefficient, and difficulties with replicating exact conditions can make the results hard to compare. Studying polycrystalline surfaces will not only provide information about several surface orientations at once, but also give information about how a more complex system behaves. Measurements of individual grains with SXRD could be achieved by using a larger angle of incidence, and thus a smaller beam footprint, but this would also increase the penetration depth, and the surface sensitivity would be significantly reduced. Instead, we want to apply a tomographic approach to distinguish the different grains and get spatially resolved Tomographic SXRD (TSXRD).

As a first step in the development of TSXRD, we have developed a measurement procedure and analysis tool for grain mapping of polycrystalline surfaces using grazing incidence XRD (GIXRD). Our measurement procedure and analysis is based on 3DXRD, which is a bulk method that can provide spatially resolved grain maps in three dimensions, together with other information, such as strain [17–19]. We also use tools from 3DXRD, ImageD11 and GrainSpotter [20,21], to identify Bragg reflections in the GIXRD data and to identify possible average grain orientations. After finding the grain orientations present at the surface, we apply a back-projection approach to reconstruct the shape and position of each grain. The result is an online surface orientation map, similar to those produced using Electron Back-Scatter Diffraction (EBSD). This map will enable the separation of surface diffraction signals from different grains, hence enabling SXRD measurements of polycrystalline samples.

This paper describes the measurement and analysis procedures for the grain mapping of polycrystalline surfaces and demonstrates the possibility to map the grains of a polycrystalline Pd sample. The smallest grain identified has a diameter very close to the width of the beam, providing an estimate of the resolution. The results are confirmed by comparing them to EBSD analyses. The resulting map is a vital step in the development of TSXRD, where subsequent analysis of the corresponding Crystal Truncation Rods (CTRs) and superstructure rods will open up the possibility to determine the atomic surface structure of the different grains of more realistic devices under working conditions.

2. Experimental details

In this example, a polycrystalline Pd crystal (Surface Preparation Laboratory, Netherlands), with a diameter of the top surface of 7 mm was studied. The sample surface was polished and had grains of 100–1000 μm in diameter. The surface was cleaned in a high-vacuum chamber by three cycles of Ar^+ sputtering (1×10^{-4} mbar Ar, 1.5 kV acceleration voltage, and 10 mA emission current) and annealing at approximately 800 °C. The sample was heated using a Boralectric heater, and the temperature was estimated by a previous calibration of sample temperature versus heating current. The sample was then kept in air at room temperature throughout the measurements. The XRD measurements were performed at the Swedish Materials Science Beamline (P21.2) [22] at PETRA III at DESY in Hamburg, using the surface diffractometer. A beam energy of 38 keV was used, along with a grazing angle of incidence of 0.09° (below the critical angle of Pd at this energy). The beam was focused to a size of 7.8×100 μm (vertical × horizontal) and the beam intensity was reduced by detuning the undulator, since the high Bragg intensity would otherwise harm the detector. The scattered X-rays were collected using a 2D detector with 2880×2880 pixels and 150×150 μm pixel size (Varex Imaging XRD 4343CT) at a distance of 743 mm from the sample.

The center-of-mass position of each measured diffraction spot can be defined by the three angles 2θ, η, and ω, as indicated in Fig. 1.

The figure also defines the two coordinate systems where the lab coordinate system (x,y,z) is defined by the direct beam while (x_s,y_s,z_s) defines the sample frame, which is tilted by the angle of incidence (μ) and rotated by the angle ω around z. Throughout the analysis, it is assumed that the z-axis is the same for both coordinate systems. In the final step of the analysis, the obtained grain orientations will be
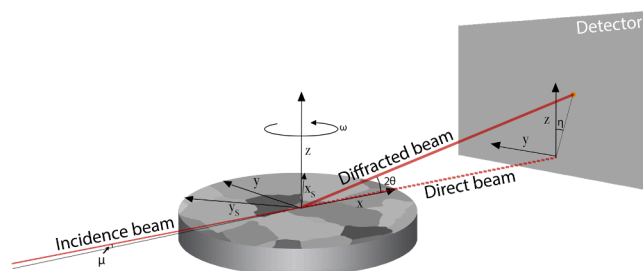
Fig. 1. Illustration of the geometry of the measurements. Two sets of reference systems are used, where (x,y,z) and (x_s,y_s,z_s) defines the laboratory and sample reference systems, respectively. The two are related through the rotation around the z axis with the angle ω, and around the y axis with the angle of incidence, μ. The center-of-mass position of each diffraction spot can be defined by the angles 2θ, η, and ω.

corrected, taking the angle of incidence (which is also the angle between z and z_s) into account. This will be a minor correction since the angle of incidence is very small. The sample was moved along y beneath the rotation as further described in Section 3. During the measurements, the sample was rotated 360° around the surface normal, while continuously acquiring 720 detector images with an exposure time of 0.15 s.

The EBSD measurement was performed with an Oxford Instruments Symmetry S2 detector linked to a high-resolution field emission scanning electron microscope (FE-SEM; Tescan Mira3) at the Department of Geology at Lund University. The analytical conditions and parameters included an accelerating voltage of 20 kV, a working distance of ~15 mm, a stage tilt of 70°, the EBSP gain set to 'High', and a background defined with a collection of 128 frames. The Hough resolution was set to 60, and the band detection min/max values to 6/8. The maps were collected with a step size of 30 μm. The data collection was performed using Oxford Instruments AZtec software. The average orientation within a grain was used as the orientation of the full grain.

3. Methodology

The measurement procedure is described in Fig. 2. The sample was initially aligned, such that the sample surface was parallel to the beam, before the angle of incidence was set. The sample position was aligned with extra care ensuring that the rotation axis was at the center of the sample and that the beam crossed this point (Fig. 2A). A rotation of the sample around its surface normal, will now provide a full measurement of the reciprocal lattice in the point at the center of the sample, overlapped with data from other parts of the sample probed at certain angles during the rotation scan (Fig. 2B). By shifting the sample slightly via a translation motor under the rotational stage, such that the beam is moved off the center of rotation, different regions of the sample are probed (Fig. 2C-D). The full measurement includes 360° rotations between stepwise shifts of the sample such that the beam position moved from one edge to the other in steps as wide as the width of the beam, which for these measurements was 100 μm. This provides data from each point of the sample at all angles (see Fig. 2E-F and consider the width of the beam being similar to the step size). A full rotation or a full translation from edge to edge is not required since it will result in duplicates of measurements, but it can positively impact the certainty of the analysis.

For the analysis, each image in the scan is loaded, and a background, defined by the median of a selection of images multiplied with a correction term (max(I)/μ(I), where I is the intensity and μ(I) is the mean of I) for non-uniformities in the total intensity profile, is removed. The actual analysis is then performed, partially using available 3DXRD software, in the following steps:
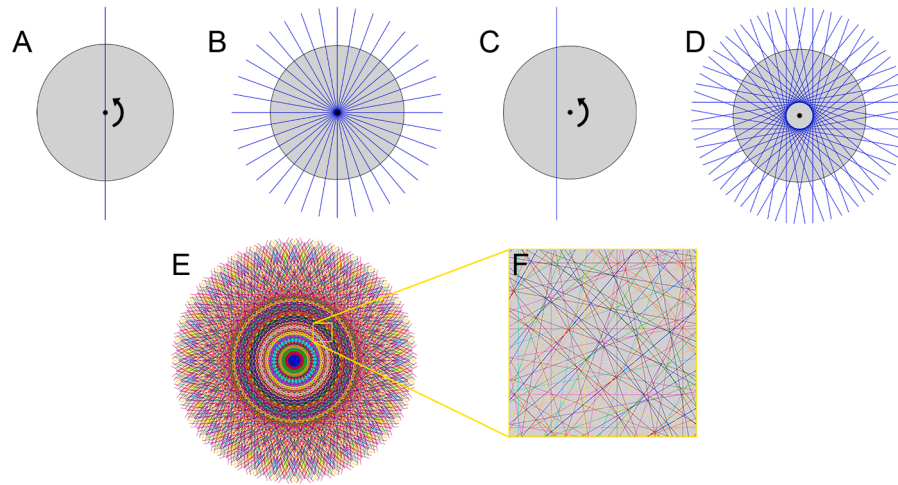
Fig. 2. Measurement procedure for TSXRD. (A) In grazing incidence XRD, the small angle of incidence results in a long beam footprint that probes a line on the surface. When measuring, the sample is rotated around its surface normal, and a large range of angles are probed (B). Only a spot at the rotational axis is probed at all angles. (C) In order to probe other parts of the surface, the sample is shifted such that the beam is at an offset from the rotational axis, before the rotation, resulting in new parts of the sample being probed at different angles (D). (E) The complete measurement consists of sample rotations at a range of offsets from the rotational axis. The different colors of the lines are from rotations at different offsets. (F) A zoom-in of the area in the yellow box shows all the beams that probe this area.

1. **Identification of G vectors.** ImageD11 [20] is applied to identify diffraction spots in the series of detector images. The corresponding reciprocal scattering vector, or **G** vector, is calculated for each diffraction spot. Since ImageD11 is adapted to diffraction data from a large beam, illuminating the full sample throughout the rotation, the scattering vectors are adjusted accordingly. Since the crystallographic phase of the sample is known, the lengths of the corresponding **G** vectors (or, equivalently, their 2θ angles) are known, and vectors outside expected ranges are discarded. This is achieved by selecting a 2θ-range from below the value of the innermost Debye-Scherrer ring and outside the last Debye-Scherrer ring of interest.

2. **Grouping G vectors.** Since the same **G** vector will be measured at multiple shifts of the beam, if a grain is wider than the beam width, all **G** vectors close to each other are grouped via thresholds on sample position in the y-direction, 2θ, η, and ω. An average **G** vector of the group is then assigned to a Debye-Scherrer ring, and **G** vectors not within a 2θ-threshold of the expected ring values are removed.

3. **Identifying grains.** An initial set of grains is found using GrainSpotter [21], which identifies grains with a set of **G** vectors. GrainSpotter provides information about the center of mass position and the optimized orientation in Euler angles for the grains. GrainSpotter was operated using the averaged **G** vectors and suitable parameters set for Euler step, uncertainties in 2θ, η, and ω, etc.

4. **Checking grain completeness.** PolyXSim [23] is used to calculate expected **G** vectors for given grain orientations. A measure of the quality of a measurement of a certain grain is its completeness, which is the number of associated measured **G** vectors compared to the expected number of **G** vectors, $C = \frac{N_{measured}}{N_{expected}}$. A threshold for the completeness is used to distinguish real orientations from other orientations with some overlapping peaks, so-called pseudo-twins.

5. **Finding unassigned G vectors.** In step 3, the set of **G** vectors we assign to a grain is the average **G** vectors from step 2. Now using the full set of measured **G** vectors, $\mathbf{G}_{total}$, we find **G** vectors within a threshold (2θ, η, and ω) of the expected **G** vectors for a grain, $\mathbf{G}_{expected}$, and assign them to the grain. The **G** vectors assigned to the grain that do not overlap in the sample space with a set minimum of other assigned **G** vectors are unassigned. All **G**

vectors still assigned to the grain are removed from $\mathbf{G}_{total}$. Repeating this for all the grains found in step 3, leaves a new set of unassigned vectors.

6. **Iterating the process.** Steps 2–5 are now repeated for the remaining **G** vectors until no more grains are found.

7. **Removing duplicate grains.** The same grain can be found more than once with different sets of **G** vectors, so once the full range of grains are extracted, they are checked for duplicates, defined by thresholds on the difference in grain orientation and center of mass position. Of the duplicates, the grain with the highest quality is kept, where quality is defined as $N_{measured}/\delta$, where δ is the average internal angle, defined as the angle between the theoretical and experimental scattering vectors.

8. **Identifying grains by mapping the completeness.** For each identified grain, the corresponding **G** vectors within thresholds of $\mathbf{G}_{expected}$ vectors are selected. Each **G** vector can be projected into the sample space as the footprint of the X-ray beam that resulted in the corresponding diffraction spot, since the offset from the sample center and the rotation angle are known. All footprints for one grain are then made into a density map, where each overlap of the footprints gives an increase in intensity. The overlap can show the grain position, as shown in Fig. 3.

The density (i.e., the number of overlapping **G** vectors), d_{map}, is normalized against the expected number of **G** vectors so that we instead map the completeness, C_{map}, of the grain in each point of the surface. This completeness is now defined as $C_{map}=d_{map}/N_{expected}$. The maximum of C_{map} is not necessarily the same as C, as defined above, since the $\mathbf{G}_{measured}$ includes all identified **G** vectors belonging to this grain, while these may not come from the same point in the grain. Grains, where the maximum of C_{map} is too low, are removed, since a low overlap of vectors in the sample space indicates that the **G** vectors are not from a real grain. After this, a Gaussian filter is applied to smooth the density map.

The grain is now extracted from the completeness map as all pixels where $C_{map} > T \times \max\left(C_{map}\right)$, where T is a set threshold. Larger grains will, in general, have higher intensity since the larger area measured by the beam will contribute to better completeness. That large grains grow, and small grains shrink or disappear has also been seen in 3DXRD [19]. Our approach to minimize this effect is to normalize the final completeness map of each grain by:
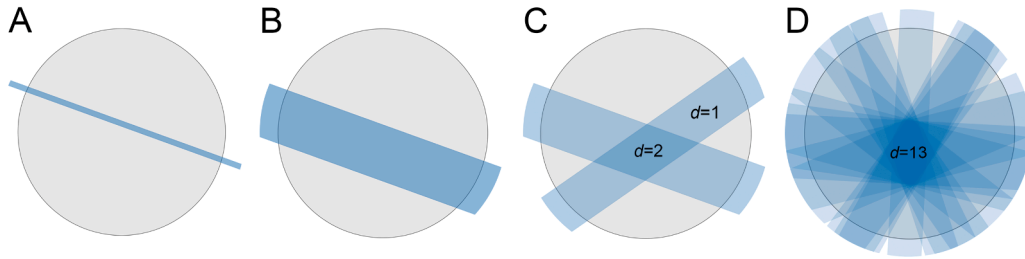
Fig. 3. Illustration of density map. (A) The incoming X-ray beam resulting in a diffraction spot of one expected **G** vector . (B) A grain larger than the beam width will result in a multiplicity of the same **G** vector at more than one shift of the sample. Here all X-ray beams producing in the same **G** vector are shown. (C) Overlapping the beams corresponding to more **G** vectors assigned to the same grain will result in a density map, where d is the density. (D) As more vectors are included (here, 13 **G** vectors), we can start to distinguish the grain shape. If $N_{expected}=13$, the completeness is $C_{map}=1$.

$$C_{final} = \frac{C_{map}}{\sqrt{\max\left(C_{map}\right)\sqrt{r}}},$$

where r is the approximate radius of the extracted grain, assuming a perfectly circular grain.

9. **Mapping the sample surface.** The completeness map of each grain is converted to a matrix with a pixel size smaller than the beam width. Pixels outside of the sample boundaries are set to 0. Many of the grains will now overlap, and to assign each pixel to a specific grain, the completeness of each grain is compared in each pixel. The grain with the highest completeness is chosen for each pixel.

10. **Removing small grains.** The beam width limits the spatial resolution of the method. Grains with an area smaller than D^2, where D is the beam width, are removed, and the corresponding pixels are instead assigned to the grain with the most neighboring pixels.

11. **Combining split grains.** To combine grains split into pieces, neighboring grains with orientation differences within a set threshold are combined, using the orientation of the highest quality grain as the orientation of the combined grain.

12. **Correcting for sample tilt.** The orientations of the grains are corrected for the surface tilt from the grazing angle of incidence by applying a rotation matrix to the orientation matrices.

4. Results and discussion

To demonstrate the grainmapping with grazing incidence XRD, we measured a Pd polycrystal with grains of different orientations and sizes using a 7.8×100 μm X-ray beam. The sample was scanned sideways such that the beam position moved from edge to edge in 100 μm steps (in total 73 steps). In each step, the sample was rotated 360° while continuously acquiring 720 detector images, i.e. with 0.5° intervals. As an example, Fig. 4 shows the rotational scan, where the beam crossed the center of rotation, which is also the center of the sample, and all the detector images are combined by showing the highest intensity of each pixel throughout the scan. The blue circles indicate the diffraction spots identified as originating from the grain in the center of the sample.

The following part follows the steps defined in Section 3.

1. **Identification of G vectors.** About 250 – 450 **G** vectors were identified in each of the 73 scans, resulting in a total of approximately 19 500 **G** vectors, after removal of spots outside of $-90° < \eta < 90°$ and $8.0° < 2\theta < 16.3°$ (a range from inside the first and outside the fourth Debye-Scherrer rings of Pd).

2. **Grouping G vectors.** **G** vectors that were similar, within thresholds of $y \pm 500$ μm, $2\theta \pm 0.5°$, $\eta \pm 0.18°$, and $\omega \pm 1.5°$, were grouped together. The thresholds are picked such that the range in stage position approximately corresponds to the expected average size of the surface grains, the 2θ is a range around the
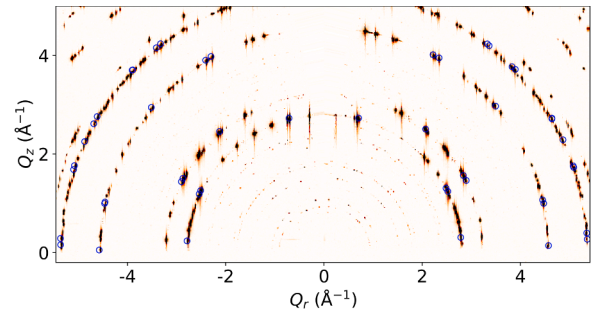
Fig. 4. The diffraction pattern of one rotational scan at the center of the sample shown as the maximum intensity for each pixel, where $Q_r = \sqrt{Q_x^2 + Q_y^2}$. Diffraction spots from a grain in the center of the sample, found by GrainSpotter, are marked with blue rings. The overlapping rings are diffraction spots that occur at different ω and will thus not overlap in 3D. The rotational range could be smaller and still be sufficient for GrainSpotter, but the overlapping peaks is an additional point of information for distinguishing the correct orientation from other orientations with similar diffraction patterns.

uncertainty of the diffraction angle, and ω is within the range of three rotational steps.

3. **Identifying grains.** GrainSpotter was run with a completeness threshold of 60 %, Euler step of 6°, and the uncertainties $\sigma_{2\theta}=0.5°$, $\sigma_\eta=1.8°$, and $\sigma_\omega=1.5°$

4. **Checking grain completeness.** Since peaks can be misassigned and noise can be assigned as a **G** vector, there is no certain threshold to completely remove pseudo-twins without risking the loss of real grains. However, a threshold of 60 % is reasonable and around the limit where it is expected to remove most pseudo-twins, even with maximum overlap of spots.

5. **Finding unassigned G vectors.** The threshold for assigning **G** vectors to a grain and removing them during the iterative GrainSpotter procedure were $2\theta \pm 0.5°$, $\eta \pm 1.1°$, and $\omega \pm 1.0°$

6. **Iterating the process.** Steps 2–5 were iterated 16 times.

7. **Removing duplicate grains.** Duplicates were defined as grains below a 0.15° orientation difference and 200 μm position difference, which removed three grains, leaving 64 grains.

8. **Identifying grains by mapping the completeness.** For the completeness map, **G** vectors within $2\theta \pm 0.5°$, $\eta \pm 1.1°$, and $\omega \pm 1.0$ of an expected **G** vector were used. The density map of one of the grains can be seen in Fig. 5A, where the contour of the grain can be observed. Grains with a maximum map completeness <0.3 were removed, resulting in 53 remaining grains. The contour of the grains was defined with $T = 45$ %. An example of a grain contour can be seen in Fig. 5B.

9. **Mapping the sample surface.** The completeness maps of all grains were combined in a 720×720 matrix.
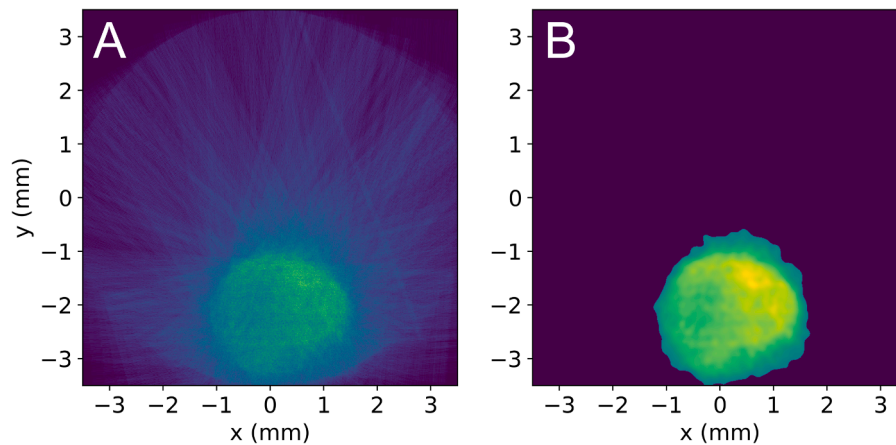
Fig. 5. Identification of a grain from the density map. (A) The density map of one grain is shown as each beam of a corresponding G vector over the sample space. The intensities of overlapping beams are summed. (B) The grain after Gaussian smoothing removing intensity where the density map has C < 0.45.

10. **Removing small grains**. After the completeness maps were combined and grains with a size smaller than the beam size were removed, 39 grains remained. It is worth noting that the diffraction of grains smaller than the beam can still be measured, and the smaller grains removed in this step can be real surfaces. Hence, if the purpose is to detect which surfaces exist, then this step could be disregarded. For the purpose of mapping the surface, however, our approach cannot determine the position and shape of the grains smaller than the beam width.

11. **Combining split grains.** The remaining grains were checked for split grains defined as neighboring grains (within 5 pixels distance) and with orientation shift <1.7° The split grains could

stem from orientation variations within a grain, but with this threshold, the variations are within our uncertainty limits, and the splits are assumed to be caused by errors in the analysis. The final map contains 30 grains.

12. **Correcting for sample tilt.** With our angle of incidence of 0.09°, the correction is well below other uncertainties, but could be of importance, especially if the incidence angle is larger.

The optimized Euler angles identified by GrainSpotter can be used to visualize the grains as an inverse pole figure map, as shown in Fig. 6A. The figure also shows approximate surface normal Miller indices for a selection of grains. This approximation assumes that the surface is a
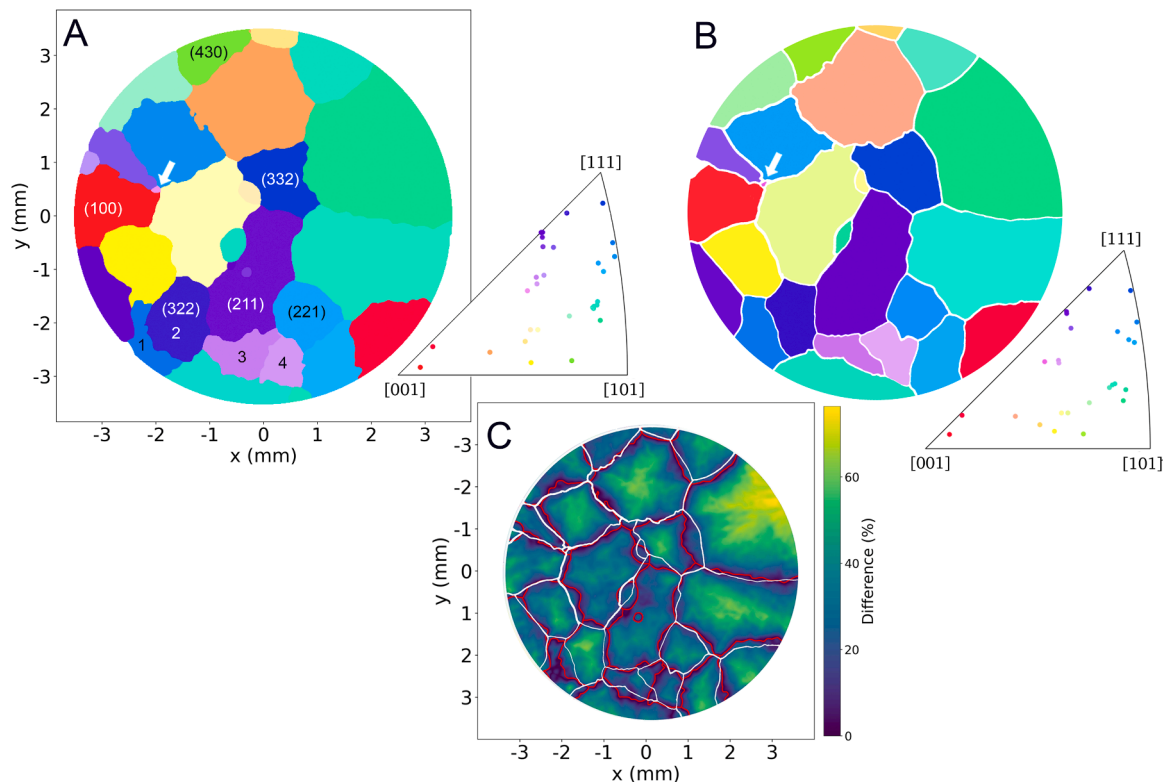
Fig. 6. The final grain map. (A) The inverse pole figure map from the grazing incidence XRD measurement, with approximate miller indices for a selection of grains. (B) The EBSD map of the same sample. The color shows the average orientation of the grain. The white arrow marks the smallest grain (120 × 100 μm). (C) The difference between the most complete grain and the second most complete grain in each pixel of the surface given as percent of the completeness of the most complete grain in that pixel. The red lines mark the grain boundaries given by SXRD and the white lines mark the grain boundaries from EBSD.

perfect cut of the bulk structure and that there is no faceting.

For comparison, Fig. 6B shows the EBSD grain map, mainly confirming the validity of the analysis above. Even the smallest grain in the EBSD map is also found using XRD (see the white arrow in Fig. 6A-B). This grain is approximately 120×100 μm, confirming the spatial resolution being defined by beam width. There are some differences in the shape of the grains; see, for instance, the grains numbered 3 and 4, and the boundary between grains 1 and 2. One reason for these differences it that the EBSD data have been treated with a standard smoothening of the grain boundaries, also removing outliers. More important, however, is the long beam footprint in GIXRD, which means that the signal of each grain is smeared out along the beam. Far away from a specific grain, only one or very few corresponding beams will overlap, and the corresponding completeness will be very low. Close to the grain, however, the overlap, and hence the completeness, might be significant. Close to the grain boundaries, the quality of the surface will also be lower, resulting in a lower completeness of the correct grain. Hence, there is an inherent uncertainty in the boundary position. To illustrate this, Fig. 6C shows the difference in completeness, in each pixel, between the two most complete grain signals, relative to the highest completeness. This is a qualitative measure of the reliability of the grain map. In addition, the grain boundaries from GIXRD and EBSD are shown in red and white, respectively. As expected, the completeness difference is small in the areas around the grain boundaries, and the boundaries defined by the two methods always stay within the areas of small completeness difference.

Comparing the orientation of the grain maps from EBSD and XRD, the difference between the same grain is between 0.2 and 3°. The average orientation difference between the two methods is 1.1°, which is approximately the orientation difference within single grains according to the EBSD measurement.

As mentioned above, the method described here is similar to 3DXRD. In 3DXRD, it is common to work with a beam as wide as the sample, such that all data is acquired during a single rotational scan [21]. These measurements are, of course, significantly faster and will provide information about the center of mass and the orientation of the grains present at the surface. We are, however, also interested in the shape of the grains, and therefore adopted the measurement method from scanning 3DXRD, as described by Hayashi et al. [19]. Their pixel-by-pixel approach, to analyze the diffraction of a small volume of the sample and find the most complete orientation, has advantages when intragranular misorientations are of interest, but the disadvantage of being time-consuming. When only the shape and average orientation of the grains are required, the back-projection approach presented here provides a faster analysis, especially for larger samples.

5. Conclusion

In this work, we have taken the first step towards TSXRD, by developing both measurement and analysis procedures for grain mapping of polycrystalline samples using an SXRD setup. The validity of the analysis is confirmed by EBSD, a more established method for mapping these kinds of surfaces. Mapping using grazing incidence XRD found all the grains found in the EBSD characterization, down to a grain just larger than the X-ray beam width and with an average surface orientation difference of 1.1°, as compared to EBSD.

If only mapping grains of surfaces and the grain orientations are of interest, EBSD is a faster and more available method. The grazing incidence of the X-ray beam also makes the grain boundaries slightly less exact. What our method can provide is grain maps with the sample mounted on the diffractometer. The grain maps can then be used to select regions (grains) on which to perform *in-situ* and *operando* SXRD measurements. The requirements for the beamline and light source are similar to those of standard SXRD measurement.

Samples of the size presented here can be measured with 100 μm resolution in 1–2 h at the beamline P21.2 at PETRA III. The development

is, however, initiated with fourth-generation synchrotrons, such as MAX IV, ESRF-EBS and the future PETRA IV, in mind. The increased brightness at these facilities will reduce the measurement time to about a minute, assuming that the sample environment can allow for fast enough rotations. As in all surface diffraction measurements, sample alignment and beam stability are crucial.

The next step in the development of TSXRD will be similar measurements, but with the Bragg reflections covered and a higher X-ray beam intensity such that the surface signal, that is, CTRs and superstructure rods, becomes visible. The intensity for the measurements presented here is reduced by detuning the undulator (similar result could be achieved by using attenuators), so the time frame of the surface measurements will be similar. Since we already have the surface grain map, we will then be able to separate the surface diffraction from different grains and determine the surface structure of each grain. When the maps of the grains of interest are known, the time resolution can also be increased, at the expense of spatial resolution, by increasing the step size. If an even higher time-resolution is desired, diffraction signals, which have been identified belonging to specific grains, can be followed by scanning SXRD, where the sample is rotated with the center of rotation at the center of mass of each grain.

TSXRD will enable SXRD studies of polycrystalline samples and, thus, *operando* measurements of more complex and more realistic samples. It can be a valuable addition to the experimental toolbox, for instance, in the fields of catalysis, electrochemistry, corrosion, batteries, and solar cells.

Code

pyTSXRD (version 1), containing the functions and Jupyter Notebook used for this analysis, is available for use at https://github.com/sjoehann/pyTSXRD.

CRediT authorship contribution statement

Hanna Sjö: Writing – review & editing, Writing – original draft, Visualization, Validation, Software, Methodology, Investigation, Formal analysis, Data curation. **Anatoly Shabalin:** Writing – review & editing, Software, Methodology. **Ulrich Lienert:** Writing – review & editing, Methodology, Investigation. **Johan Hektor:** Writing – review & editing, Methodology, Investigation. **Andreas Schaefer:** Writing – review & editing, Investigation. **Per-Anders Carlsson:** Writing – review & editing, Investigation. **Carl Alwmark:** Writing – review & editing, Investigation, Data curation. **Johan Gustafson:** Writing – review & editing, Writing – original draft, Validation, Supervision, Project administration, Methodology, Investigation, Conceptualization.

Declaration of competing interest

The authors declare that they have no known competing financial interests or personal relationships that could have appeared to influence the work reported in this paper.

Beamline (P21.2). Beamtime was allocated through the long-term project 20220011.

Data availability

Data will be made available on request.

References

[1] S. Chavez, B. Werghi, K.M. Sanroman Gutierrez, R. Chen, S. Lall, M. Cargnello, Studying, promoting, exploiting, and predicting catalyst dynamics: the next frontier in heterogeneous catalysis, J. Phys. Chem. C 127 (2023) 2127–2146, https://doi.org/10.1021/acs.jpcc.2c06519.

[2] J.K. Nørskov, A. Latimer, C.F. Dickens (Eds.), Research needs towards sustainable production of fuels and chemicals, 2019, https://www.energy-x.eu/research-needs-report/.

[3] I. Hut, L. Matija, M. Peric, P. Nikolovski, S. Pelemis, et al., Nanomaterials for sustainable energy production and storage: present day applications and possible developments, in: D. Brabazon, et al. (Eds.), Commercialization of Nanotechnologies–A Case Study Approach, Springer, Cham, 2017, pp. 31–72, https://doi.org/10.1007/978-3-319-56979-6_3.

[4] X. Nie, Z. Zhang, H. Wang, X. Guo, C. Song, Effect of surface structure and Pd doping of Fe catalysts on the selective hydrodeoxygenation of phenol, Catal. Today 371 (2021) 189–203, https://doi.org/10.1016/j.cattod.2020.07.038.

[5] C.J. Bondeu, M.T.M. Koper, Electrochemical reduction of the carbonyl functional group: the importance of adsorption geometry, molecular structure, and electrode surface structure, J. Am. Chem. Soc. 141 (30) (2019) 12071–12078, https://doi.org/10.1021/jacs.9b05397.

[6] F. Schiller, M. Ilyn, V. Pérez-Dieste, C. Escudero, C. Huck-Iriart, N.Ruiz del Arbol, B. Hagman, L.R. Merte, F. Bertram, M. Shipilin, S. Blomberg, J. Gustafson, E. Lundgren, J.E. Ortega, Catalytic oxidation of carbon monoxide on a curved Pd crystal: spatial variation of active and poisoning phases in stationary conditions, J. Am. Chem. Soc. 140 (47) (2018) 16245–16252, https://doi.org/10.1021/jacs.8b09428.

[7] G. Ertl, Reactions at surfaces: from atoms to complexity (Nobel lecture, Angew. Chem. Int. Ed. 47 (2008) 3524–3535, https://doi.org/10.1002/anie.200800480.

[8] C. Smith, A.K. Hill, L. Torrente-Murciano, Current and future role of Haber–Bosch ammonia in a carbon-free energy landscape, Energy Environ. Sci. 13 (2020) 331–344, https://doi.org/10.1039/C9EE02873K.

[9] O. Karslıoğlu, H. Bluhm, Ambient-pressure X-ray photoelectron spectroscopy (APXPS), in: J. Frenken, I. Groot (Eds.), Operando Research in Heterogeneous

[10] P. Winkler, J. Zeininger, Y. Suchorski, M. Stöger-Pollach, P. Zeller, M. Amati, L. Gregoratti, G. Rupprechter, Coexisting multi-states in catalytic hydrogen oxidation on rhodium, Nat. Commun. 12 (2021) 6517, https://doi.org/10.1038/s41467-021-26855-y.

[11] T. Franz, B. von Boehn, H. Marchetto, B. Borkenhagen, G. Lilienkamp, W. Daum, R. Imbihl, Catalytic CO oxidation on Pt under near ambient pressure: a NAP-LEEM study, Ultramicroscopy 200 (73–78) (2019) 0304–3991, https://doi.org/10.1016/j.ultramic.2019.02.024.

[12] M. Salmeron, B. Eren, High-pressure scanning tunneling microscopy, Chem. Rev. 121 (2) (2021) 962–1006, https://doi.org/10.1021/acs.chemrev.0c00429.

[13] G.S. Harlow, E. Lundgren, M. Escudero-Escribano, Recent advances in surface x-ray diffraction and the potential for determining structure-sensitivity relations in single-crystal electrocatalysis, Curr. Opin. Electrochem. 23 (162–173) (2020) 2451–9103, https://doi.org/10.1016/j.coelec.2020.08.005.

[14] U. Hejral, M. Shipilin, J. Gustafson, A. Stierle, E. Lundgren, High energy surface x-ray diffraction applied to model catalyst surfaces at work, J. Phys. Condens. Matter 33 (2020) 073001, https://doi.org/10.1088/1361-648X/abb17c.

[15] A. Stierle, J. Gustafson, E. Lundgren, Surface-sensitive x-ray diffraction across the pressure gap, in: J. Frenken, I. Groot (Eds.), Operando Research in Heterogeneous Catalysis. Springer Series in Chemical Physics, Springer, Cham, 2017, pp. 59–87, https://doi.org/10.1007/978-3-319-44439-0_3, vol 114.

[16] P.L.J. Gunter, J.W. (Hans) Niemantsverdriet, F.H. Ribeiro, G.A. Somorjai, Surface science approach to modeling supported catalysts, Catal. Rev. 39 (1–2) (1997) 77–168, https://doi.org/10.1080/01614949708006469.

[17] H.F. Poulsen, Three-dimensional x-ray diffraction microscopy: mapping polycrystals and their dynamics, Springer Tr. Mod. Phys. 205 (2004) 51–72.

[18] H.F. Poulsen, 3DXRD: grain maps, grain dynamics and grain refinements, Crystallogr. Rev. 10 (1) (2004) 29–43, https://doi.org/10.1080/08893110410001664918.

[19] Y. Hayashi, Y. Hirose, Y. Seno, Polycrystal orientation mapping using scanning three-dimensional X-ray diffraction microscopy, J. Appl. Cryst. 48 (2015) 1094–1101, https://doi.org/10.1107/S1600576715009899.

[20] ImageD11, https://sourceforge.net/p/fable/wiki/imaged11/, 2017 (accessed 2024-09-09).

[21] S. Schmidt, GrainSpotter: a fast and robust polycrystalline indexing algorithm, J. Appl. Cryst. 47 (2014) 276–284, https://doi.org/10.1107/S1600576713030185.

[22] Z. Hegedüs, T. Müller, J. Hektor, E. Larsson, T. Bäcker, S. Haas, A.L.C. Conceiçao, S. Gutschmidt, U. Lienert, Imaging modalities at the Swedish materials science beamline at PETRA III, IOP Conf. Ser.: Mater. Sci. Eng. 580 (2019) 012032.

[23] PolyXSim - 3DXRD far-field simulation of polycrystals, https://sourceforge.net/p/fable/wiki/PolyXSim/, 2016 (accessed 2024-09-09).